

Article

Structure from Motion Point Clouds for Structural Monitoring

Fausto Mistretta, Giannina Sanna , Flavio Stochino *  and Giuseppina Vacca 

Department of Civil, Environmental Engineering and Architecture, University of Cagliari, 09123 Cagliari, Italy

* Correspondence: fstochino@unica.it; Tel.: +39-070-675-5115

Received: 3 June 2019; Accepted: 15 August 2019; Published: 20 August 2019



Abstract: Dense point clouds acquired from Terrestrial Laser Scanners (TLS) have proved to be effective for structural deformation assessment. In the last decade, many researchers have defined methodology and workflow in order to compare different point clouds, with respect to each other or to a known model, assessing the potentialities and limits of this technique. Currently, dense point clouds can be obtained by Close-Range Photogrammetry (CRP) based on a Structure from Motion (SfM) algorithm. This work reports on a comparison between the TLS technique and the Close-Range Photogrammetry using the Structure from Motion algorithm. The analysis of two Reinforced Concrete (RC) beams tested under four-points bending loading is presented. In order to measure displacement distributions, point clouds at different beam loading states were acquired and compared. A description of the instrumentation used and the experimental environment, along with a comprehensive report on the calculations and results obtained is reported. Two kinds of point clouds comparison were investigated: Mesh to mesh and modeling with geometric primitives. The comparison between the mesh to mesh ($m2m$) approach and the modeling (m) one showed that the latter leads to significantly better results for both TLS and CRP. The results obtained with the TLS for both $m2m$ and m methodologies present a Root Mean Square (RMS) levels below 1 mm, while the CRP method yields to an RMS level of a few millimeters for $m2m$, and of 1 mm for m .

Keywords: structural health monitoring; structure from motion; terrestrial laser scanner; close-range photogrammetry; point clouds modeling

1. Introduction

Structural Health Monitoring is one of the main objectives of engineering surveys [1] and it is particularly important for buildings, bridges, dams, or other infrastructures subjected to extreme events such as earthquakes, hurricane, flooding, fire [2,3], or due to natural aging [4,5]. For this reason, periodic monitoring of the structural condition is necessary in order to ensure and maintain the safety and functionality of buildings and infrastructure [6–14]. Sometimes it is sufficient to measure the eigenfrequency variations along the lifecycle of the structure. In other cases, it is important to control and record displacements and deformations even if it requires quite complex monitoring systems. Geomatic techniques often represent an effective approach and the changes in time of target point coordinates is the core of the method. Thus, knowledge of the typology, characteristics, and scale of the structural deformations is essential for an accurate measurement of permanent damage [15].

Currently, the geometrical survey of objects (buildings, bridges, and/or other structures) can be easily obtained with dense point clouds. Also, structural monitoring may be developed using this approach. Until a few years ago, Terrestrial Laser Scanner (TLS) was the only technique widely used to generate dense point clouds. Interesting reports on point clouds from TLS assessing changes and deformations can be found in [16–18]. Deformation analysis can be developed at the level of

single-point location (point-wise [19]) or at the object level (see [20,21]). In [22], in order to identify seismic-induced building deformations, the notion of morphological maps is introduced.

The measure of deformation is often obtained through the fusion of data collected by different sensors. In [23–25], the laser scanner data are merged with data obtained through other sensors; in [26,27], laser scanner data, acquired from different platforms, are combined together.

Structural monitoring based on TLS has been studied in detail in the literature. In [28], damage detection and volume change analysis for a full-scale structural test are obtained using a terrestrial laser scanner. In [22] and [29], the deformations of several ancient towers are analyzed by TLS and the Finite Element Method (FEM). The structural health condition of historical arch bridges is assessed by FEM and a combined use of TLS and Close-Range Photogrammetry (CRP) in [30]. Additionally, monitoring of moving rotor blades of windmills is reported in [31]. In [32], dam deformations are measured using TLS.

The use of point clouds to monitor or control structural deformations involves three challenges. First, the difficulty in managing big data. Secondly, it is impossible to scan the same point at different epochs and finally, the data itself is affected by the instrument's noise [33]. The first problem is solved by segmentation, the second through the insertion of specific targets or cloud-to-cloud comparison solutions, while the third problem may be mitigated through interpolation models [9]. In this work, in order to compare point clouds at different epochs, the latter two solutions were tested: Cloud to cloud comparisons and interpolation models. These two methodologies have already been discussed in different papers, especially with the use of TLS [10,11,22,34,35]. The “point to mesh” and “mesh to mesh” methods have been applied and studied in [36]. Other authors have developed a model of the surface of the deformed object. They proved that this approach is capable of assessing the object's behavior with a lower influence of measurement noise: [22,37]. In [38,39], a summary of the TLS performance for several objects is also presented.

The behavior of a slender beam is often described by the Euler–Bernoulli model. In this approach, the static deformed shape can be obtained from a 2nd order linear ordinary differential equation, which enforces the equilibrium condition, obtaining a simple relationship between the bending moment and the curvature. The solution of this equation is a polynomial function whose degree depends on the loading conditions.

In [38], Tsakiri presents an overview of the different functions modeling several kinds of objects measured with TLS. In particular, he reports the case of a wooden beam where it is proved that the best function representing beam deflection is a third-degree polynomial. Also, in [39], the case of a wooden beam modeled with a third-degree polynomial is reported, while in [35], the model of a steel beam is obtained using a second-degree polynomial.

Dense point clouds obtained by photogrammetry [40] have become useful in monitoring thanks to the development of Structure from Motion (SfM) algorithms (see [41–44]).

The state-of-the-art of dense image-matching is discussed in [45], where a comparison of the available software is also presented. Most of the published studies (see [45–48]) estimate the accuracy of the point cloud through the use of targets or through sections extracted from the cloud and compared with the design ones. Some interesting examples of archeology and cultural heritage preservation based on point cloud surveys are presented in [49–51]. In [52], a critical review of the developments in automated image processing is discussed. It is also possible to track 2D displacements in rectified images with acceptable accuracy, without going through 3D reconstruction, see [53,54].

In this work, the models traditionally used for deformation monitoring with TLS point clouds were applied to dense point clouds obtained from CRP.

The main target of this research was to evaluate the accuracy and precision that can be obtained by CRP point clouds measuring structural deformations. The case study involved two Reinforced Concrete (RC) beams, tested under four-points bending loading conditions. The displacements were measured using a standard Displacement Transducer (DT), TLS, and CRP. Preliminary results obtained with CRP on the first RC beam were presented in [55].

In this paper, measurement techniques and data processing of the structural deformations are shown, and a comparison between the TLS technique and the CRP is also presented.

The validation of the results was performed using two metrological instruments: The Leica AT402 Laser Tracker (LT) and the AICON MoveInspect DPA system with a Nikon D3x metric camera (DPA).

The paper is organized as follows: Section 2 presents the instruments and technologies used in the load tests of the beams. Section 3 reports the results of the measurements with TLS, CRP, and metrological instruments. The comparisons between the two techniques and the metrological measurements are reported in Section 3. Finally, the discussion of the results is developed in Section 4, while conclusions and remarks are drawn in Section 5.

2. Materials and Methods

In order to test the geomatic measurement methods presented in the introduction, several four-points bending tests were developed on two Reinforced Concrete (RC) beams (labeled beam#1 and beam#2) in the Materials Laboratory of the University of Cagliari Department of Civil, Environmental Engineering and Architecture. The tests were developed in three different steps: beam#1 first load condition; beam#1 second load condition, beam#2. The adopted concrete was characterized by a cubic compressive strength of 30 MPa, while reinforcement steel presented a nominal 450 MPa yielding strength. The beams cross-section, reinforcement distribution, and test scheme can be seen in Figure 1.

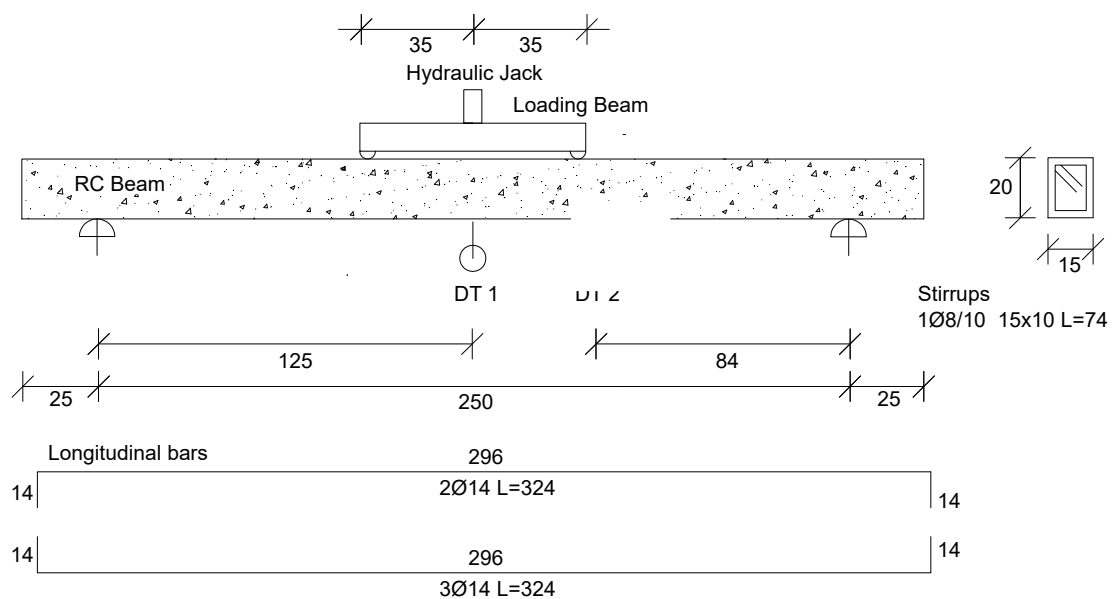


Figure 1. Reinforcement distribution, beam dimensions, and test setup (bar diameters are in mm, all other measures are in cm).

The load was applied by a hydraulic jack with quasi-static incremental steps from 0 to 68 kN and for each step, the beam displacements were measured using both TLS and CRP. The maximum load of 68 kN was selected in order to have crack openings without reaching the beam collapse condition. Details of the load conditions 1–2 for the two beams are presented in Tables 1–3.

Usually, structural displacements are measured using displacement transducers (DT) that convert rectilinear mechanical motion into a variable electric signal that can be digitally recorded, while the TLS and CRP geomatic techniques produce coordinates in a 3D reference system.

A DT was applied under the beam midspan section. Its nominal displacement is 100 mm, nominal sensitivity 2 mV/V, sensitivity tolerance $\pm 0.1\%$, measure resolution 1 μm . Its position is also represented in Figure 1.

Table 1. Plan of the performed measurements beam#1 first load condition (LC1).

Test	Load (kN)	Measurement Time (day 1)	DT	LT	DPA	TLS	CRP
1	0	10.53	√	√	√	√	√
2	11	11.11	√	√	√	√	√
3	26	11.36	√	√	√	√	√
4	40	12.01	√	√	√	√	√
5	54	12.32	√	√	√	√	√
6	68	13.08	√	√	√	√	√

Table 2. Plan of the performed measurements beam#1 second load condition (LC2).

Test	Load (kN)	Measurement Time (day 2)	DT	LT	DPA	TLS	CRP
1	0	10.39	√		√	√	√
2	22	11.27	√		√	√	√
3	48	11.50	√		√	√	√

Table 3. Plan of the performed measurements beam#2.

Test	Load (kN)	Measurement Time (day 3)	DT	LT	DPA	TLS	CRP
1	0	10.26	√		√	√	√
2	19	11.02	√		√	√	√
3	39	11.29	√		√	√	√
4	0	11.48	√	√	√		
5	19	12.07	√	√	√		
6	39	12.15	√	√	√		
7	68	12.26	√	√	√	√	√

For the TLS technique, the Faro Focus 3D Terrestrial Laser Scanner was used. It is a compact scanner characterized by an operative range that varies between 0.6 and 120 m, with a ranging error of ± 2 mm for scanner–object distances between 10 and 25 m. The scans were processed using the JRC Reconstructor software v. 3.1.0 by Gexcel Ltd. For the CRP, two digital cameras were used. The first camera was a Canon Powershot S110 with a 1/1.7" sensor (1.9 mm pixel dimension), Field of View (FoV) 94.2°, and a 12 Megapixel resolution; zoom 5×: 5.2 (G) - 26.0 (T) mm (equivalent to 35 mm: 24 (G) - 120 (T) mm on a 24 mm film); the output data formats are Exif 2.3 (JPEG) and RAW (CR2 Canon original). The second digital camera was a Canon EOS M3 with a sensor CMOS 22.3 × 14.9 mm (3.7 mm pixel dimension), Field of View (FoV) 81.5°, and a 24.2 Megapixel resolution; objective EF-S 18–55 mm; the output data formats are Exif 2.3 (JPEG) and RAW (CR2 Canon original).

The images were processed using the Photoscan software by Agisoft [56,57], which implements the SfM method [58–60].

In order to validate the results and fix a vertical reference frame for photogrammetric measurements, two metrological instrumentations were used:

- The Leica AT402 Laser Tracker (LT);
- The AICON MoveInspect DPA system with a Nikon D3x metric camera (DPA).

The first one is a metrological instrument characterized by an uncertainty in the measurement of coordinates (U_{xyz}) of $\pm 15 \mu\text{m} + 6 \mu\text{m/m}$ (Maximum Permissible Error). The second has a nominal measurement accuracy of $2 \mu\text{m} + 5 \mu\text{m/m}$ (RMS), or $3 \mu\text{m} + 7 \mu\text{m/m}$ (3σ).

Both systems obtain the coordinates of targeted points with a very high precision and all the comparisons between the examined techniques (TLS and CRP) have been performed with respect to those targets.

Figure 2 presents a view of the experimental setup.



Figure 2. Experimental setup: Beam and back-up frame, Laser Tracker (LT) pointing at targets.

2.1. Measurements Methods

Although both TLS and CRP measurement techniques provide 3D positions of points, structural displacements for the considered case are expected within the vertical direction, yielding a 1D problem. Thus, an important issue is the materialization of the direction of interest. In the TLS, with the biaxial compensator switched on, the instrumental reference system includes the vertical direction, but the CRP method needs scaling and an external reference system with the vertical direction as one of the axes. The problem for CRP remains a 3D one because the sought displacement does not necessarily lie on the longitudinal beam plane. In order to fix a common reference frame containing one vertical axis, six special aluminum targets (Figures 3 and 4), named FT#, treated with retro-reflective paint, and whose center coordinates could be measured with LT, DPA system, and CRP, were fixed in the area of the laboratory that was not subjected to variable loads.



Figure 3. Circular targets whose center coordinates were measured with both LT, inserting the prism into the central housing, and photogrammetric systems DPA (AICON MoveInspect DPA system with a Nikon D3x metric camera) and CRP (Close-Range Photogrammetry).

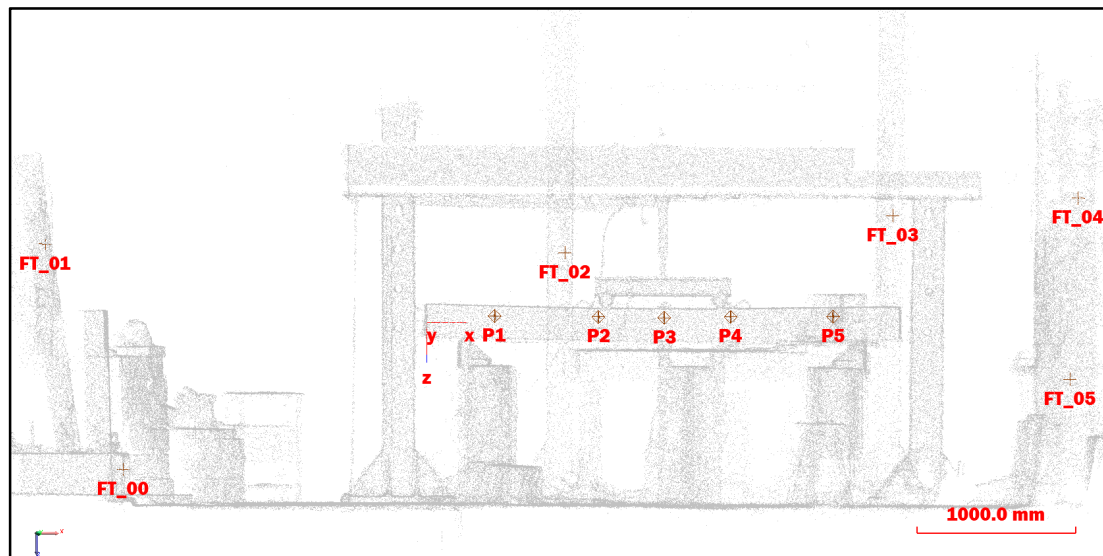


Figure 4. FT Targets and LT prism (P) location in the laboratory.

The six FT targets were measured multiple times to check the stability of both the reference frame and the LT instrument.

In order to measure the beam displacements, five laser tracker prisms (P#) were fixed on the front side—corresponding to the compressed part of the cross-section—to avoid triggering cracks during the test. The prisms (P#) were placed at both ends of the beam (P1 and P5), on the midspan section (P3) and at 1/3 and 2/3 of the beam span (P2 and P4). Their positions are also depicted in Figure 4.

A large set of photogrammetric retro-reflecting targets were spread all over the measurement area, according to the following list:

- 78 CTs (Coded Targets), nine of which are part of the AICON reference system (calibrated cross and bars);
- 36 UTs (Uncoded Targets), four of which are part of the AICON reference system.

Out of the 114 points, 41 were positioned outside the load area in order to establish and verify the reliability of the outcomes. Another 33 targets were placed on the beam, five of which were along the cross-section corresponding to the Laser Tracker P# points. Figure 5 shows the spatial distribution of the targets in the whole test area.

The LT was stabilized in a fixed position during the measurement sessions and remotely controlled using the Spatial Analyzer (SA) software by New River Kinematics.

In each load condition of the beam, the DPA survey was performed and processed with the AICON 3D Studio software. In each survey, the coordinates of all the targets in AICON's own internal reference system were calculated, along with their precisions. Afterwards, all the coordinate sets were transformed into the LT coordinate system through the FT# points.

TLS measurements were performed under logistic constraints which prevented the chance of moving the instrument and covering the hidden areas with multiple scans. Thus, after several tests, the TLS was located about 3 m away from the beam, in a position where the contour of the front face of the beam could be fully reconstructed (see Figure 5). An estimate of the downward displacement can be obtained by comparing each set of measurements to the reference one. Figure 6 shows the positions of the TLS and of the LT with respect to the beam.

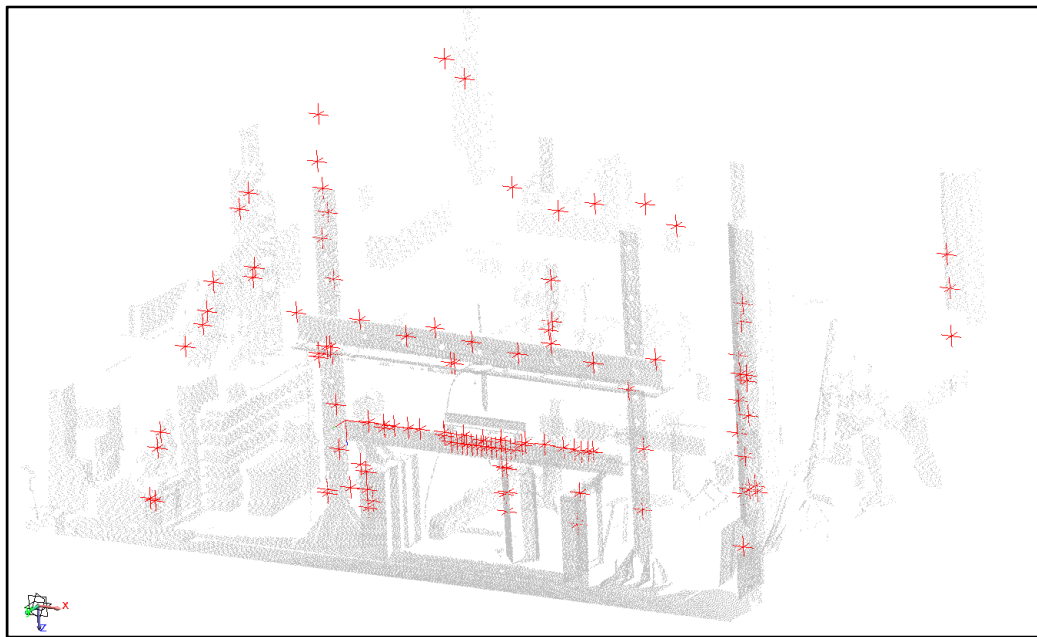


Figure 5. Spatial distribution of the targets in the test area.

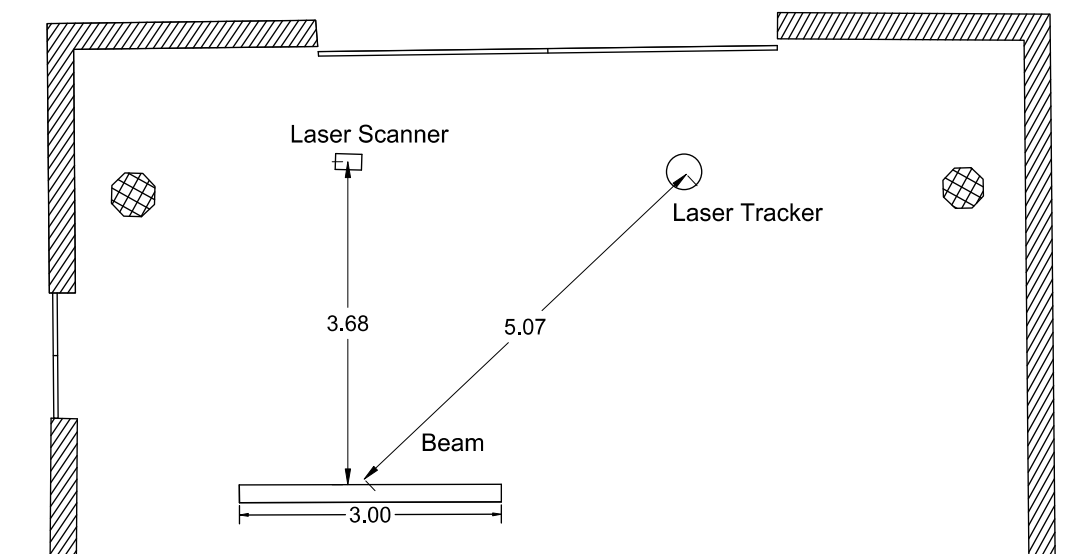


Figure 6. Plan view of the experimental instruments, distances are in meters.

During the measurement process, it was assumed that the TLS remained stationary in measuring position. Nevertheless, before each series of measurements, a scan at 360° to capture walls and other objects of the laboratory that were stable over time was run.

Images were taken at distances of between 1 and 2 m with the optical axis orthogonal to the longitudinal plane of the beam, so that the downward displacements were close to the image plane. The Ground Sample Distance (GSD) was 0.71 mm using the Powershot S100 digital camera and it was 0.41 mm using the EOS M3.

The images were processed on an HP Z420 workstation with 64 GB RAM, Intel Xeon E5-16200 3.60 GHz CPU, and NVIDIA Quadro K2000 video card.

The image-processing workflow, according to Agisoft Photoscan software, follows the standard steps of SfM software with the Bundle Adjustment on key points generating a sparse point cloud, external orientation, and generation of the dense point cloud.

The images were georeferenced using the same six FT# targets used for the DPA measurements.

2.2. Methodologies Comparison

In order to evaluate the accuracy of TLS and CRP, the displacements estimated with these methods were compared with the ones obtained from the LT and DPA.

Preliminarily, the vertical displacements from DT, LT, and DPA were compared. The comparison was performed on the P1 through P5 points placed on the beam (see Figure 5). These comparisons are referred to as LT-DPA and LT-DT hereafter in the paper.

Regarding TLS and CRP, starting from point clouds, two kinds of processing methods were investigated:

- mesh to mesh comparison ($m2m$);
- modeling with polynomials (m) and comparison of the beam deflection at each load step.

While the first one is usually implemented in commercial software, the second one is not common and depends on the shape of the scanned object. For the $m2m$ comparison, the z coordinate of the points corresponding to those of the DPA photogrammetry were obtained, reconstructing the cross sections of each mesh and extracting the z value of the surface.

In the modeling strategy, since the front face of the beam was very similar to a regular rectangle, the superior edge of the longitudinal section was modeled with a second-order polynomial. This approach was used for both TLS point clouds and CRP point clouds. To reduce each dataset (DPA included) in two dimensions, a Beam Reference System (BRS) with the following constraints was built:

- origin contained in the left-end of the beam;
- z axis vertical and pointing down;
- x axis lying on the front face of the beam (parallel to the beam longitudinal axis);
- y axis forming a right-handed system with the other two.

Figure 7 presents the position of the reference system on the beam.

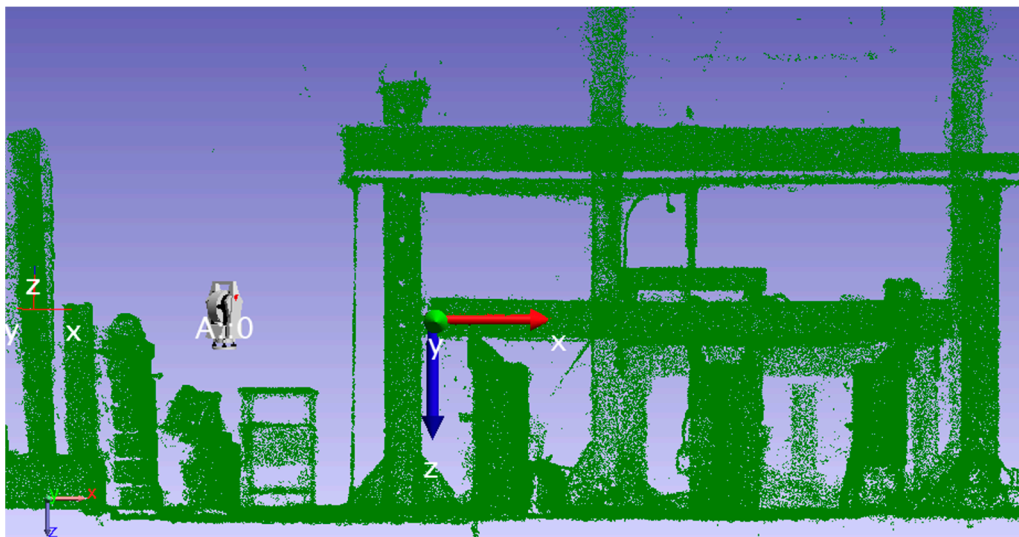


Figure 7. The reference system on the beam.

In order to compare the TLS and CRP displacements of the point clouds with the DPA displacements, the latter have been transformed in the BRS. After the extraction of the coordinates of the beam top-edge points, a least-squares fitting with a second-order polynomial was estimated to obtain the beam deflection along the beam span.

Given the x coordinate of the AICON DPA targets (see Figure 4), it was possible to calculate the z coordinate using the polynomials representing beam deflection.

The downward displacements were calculated as the difference between the z coordinates at the initial zero load and the z coordinates under the considered load step.

The comparisons of the CRP displacements measured on the meshes with the DPA ones are labeled $CRP_{Cloud(m2m)}-DPA$. Similarly, the comparison between CRP displacements obtained after polynomial modeling with the DPA displacements is labeled $CRP_{Cloud(m)}-DPA$. Likewise, for the TLS displacements, comparisons are labeled as $TLS_{(m2m)}-DPA$ and $TLS_{(m)}-DPA$.

The overall data processing follows the workflow depicted in Figure 8.

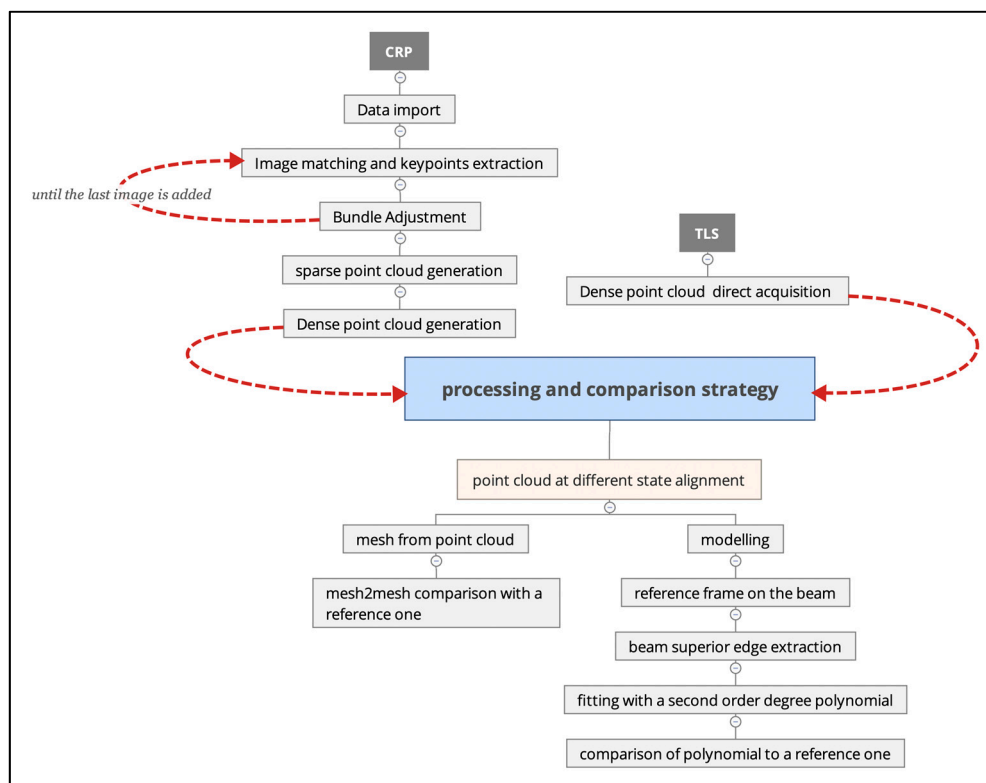


Figure 8. Processing strategy for Close-Range Photogrammetry (CRP) and Terrestrial Laser Scanners (TLS).

3. Results

Measurements started, first for beam#1 (first load condition (LC1) and second load condition (LC2)) and then for beam#2, with the instrumental observations at zero load and progressed following the load sequence of Tables 1–3. The displacement transducer remained active all the time, constantly recording displacements.

Figure 9 presents the comparison between midspan displacements of beam#1 LC1 measured by DT, LT, and DPA. Figure 10 compares midspan displacements of beam#1 LC2 measured by DT and DPA, while Figure 11 represents the case of beam 2 considering DT, LT, and DPA. For the latter case, only the second load cycle is presented. Different structural performances of the two beams can be explained, considering that beam 1 was not completely straight along its longitudinal axis; this produced different displacements along the vertical direction in comparison with beam 2. On the other hand, this is negligible for the aims of the considered analysis.

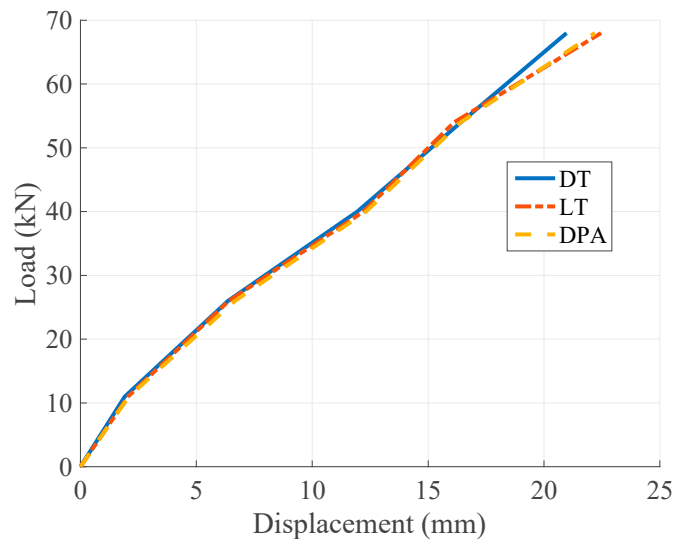


Figure 9. Displacements comparison for beam#1 LC1.

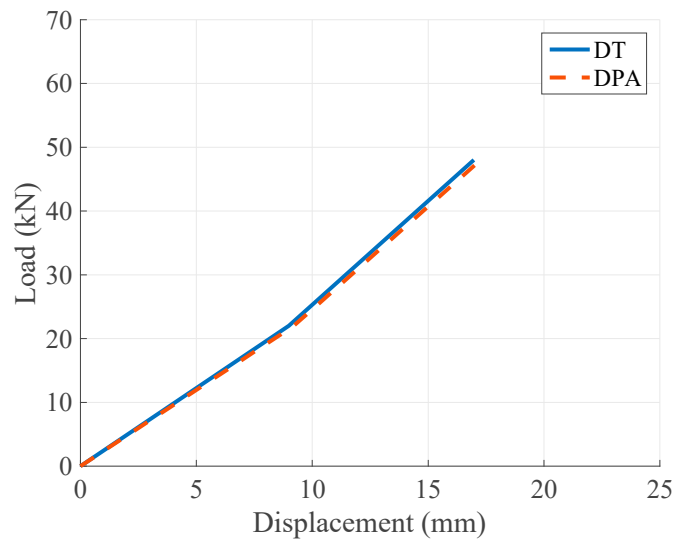


Figure 10. Displacements comparison for beam#1 LC2.

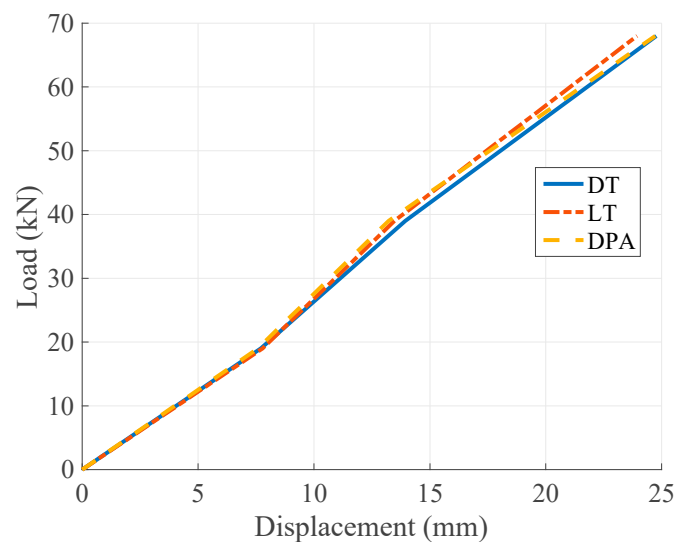


Figure 11. Displacements comparison for beam#2.

The small differences between DT and DPA that can be seen in Figure 9 are probably due to a slight modification of the correct position of the DT due to beam deflection. Instead, the differences between LT and DPA are negligible.

Tables 4 and 5 report the comparison between the vertical displacement vectors measured using LT on the five points placed on the beam and the closest DPA targets (placed in the same beam cross-sections). During the test beam#1 LC2, it was not possible to use the LT and consequently, the comparison, in that case, is not reported. The overall RMS level is obtained using Equation (1), where x_i^{M1} is the coordinate of point i obtained with the method $M1$ (which can be DPA, TLS, or CRP) and x_i^{M2} is the coordinate of the same point obtained with method $M2$ (which can be DPA, LT).

$$x_{RMS} = \sqrt{\frac{1}{N} \sum_{i=1}^N (x_i^{M1} - x_i^{M2})^2} \quad (1)$$

Table 4. DPA-LT (mm) beam#1 LC1.

Load (kN)	P1	P2	P3	P4	P5
11	−0.04	−0.04	0.03	0.04	0.03
26	0.04	0.17	0.27	0.29	0.19
40	−0.03	0.00	0.11	0.08	0.07
54	−0.12	−0.01	0.29	0.38	0.09
68	−0.30	−0.25	−0.26	−0.23	0.00
Global RMS	0.15	0.14	0.22	0.24	0.10

Table 5. DPA-LT (mm) beam#2.

Load (kN)	P1	P2	P3	P4	P5
19	−0.11	−0.19	−0.2	−0.18	−0.17
39	−0.11	−0.21	−0.25	−0.18	−0.15
68	0.10	0.60	0.78	0.48	−0.06
Global RMS	0.11	0.33	0.43	0.28	0.12

The overall RMS of beam#1 LC1 comparison is 0.18 mm.

The overall RMS of beam#2 comparison is 0.32 mm. Laser tracker (LT) and DPA measurements are in good agreement; differences are small, as shown in Tables 4 and 5. Only the last measurement of beam#2 shows a larger difference, which is possibly due to a less accurate set of measurements for the DPA in that case. For the sake of simplicity, from now on, the accuracy of TLS and CRP will be evaluated only versus DPA.

3.1. Terrestrial Laser Scanner Measurements

As stated in Section 2, for each load, both a 360° scan and a high-resolution scan in a smaller window covering just the beam, were performed. During the processing, at each load-step, after a stability check of the instruments, the meshes were built and the top edges of the beam were extracted. Using a least-squares approach, these edges (composed of about 9600 points) were fitted with a second-degree polynomial. Then, the values of this fitting curve were calculated at the x coordinate corresponding to each of the 33 DPA targets on the beam, thereby obtaining the TLS z coordinate.

Tables 6–8 show the RMS values, at each load condition, for the mesh to mesh ($m2m$) and polynomial (m) methodologies.

Figure 12 shows the polynomials fitted at each load step and for beam#1 second load condition and for beam#2, see Tables 7 and 8.

Table 6. RMS (mm) of each TLS methodology with DPA beam#1 LC1.

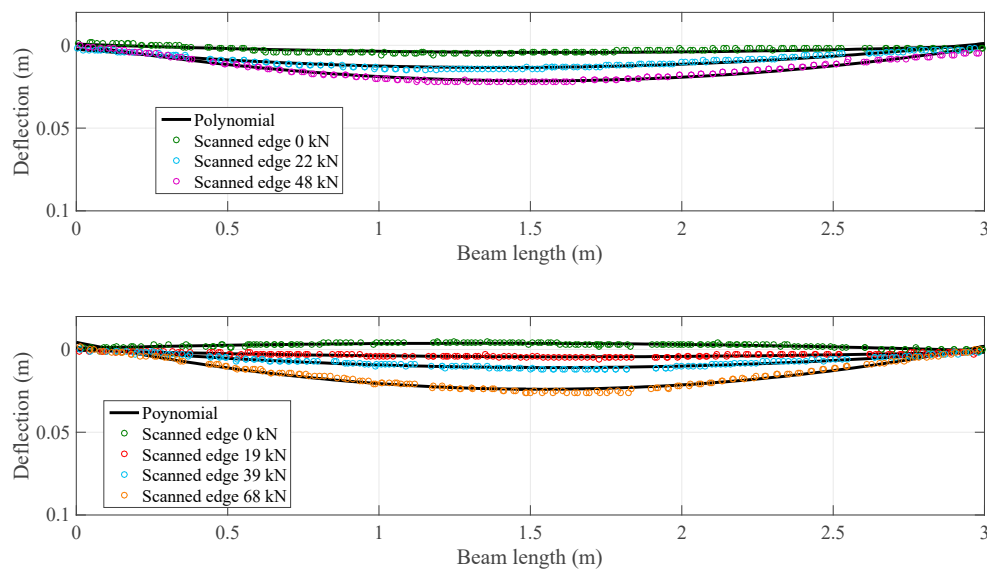
Load (kN)	TLS(m2m)-DPA	TLS(m)-DPA
11	1.01	0.38
26	0.98	0.42
40	0.97	0.60
54	0.99	0.63
68	0.92	0.62
Global RMS	0.97	0.54

Table 7. RMS (mm) of each TLS methodology with DPA beam#1 LC2.

Load (kN)	TLS(m2m)-DPA	TLS(m)-DPA
22	1.14	1.08
48	0.78	0.77
Global RMS	0.98	0.94

Table 8. RMS (mm) of each TLS methodology with DPA beam#2.

Load (kN)	TLS(m2m)-DPA	TLS(m)-DPA
19	0.54	0.58
39	0.50	0.56
68	0.95	0.76
Global RMS	0.69	0.64

**Figure 12.** Terrestrial Laser Scanners (TLS) polynomials fitted along the beam span for beam#1 LC2 (**top**) and beam#2 (**bottom**). The rounded markers represent a selection of the mesh points used in the fitting process.

3.2. CRP Measurements

The digital camera Powershot S110 was used for beam#1 LC1, while the digital camera EOS M3 was used for the beam#1 LC2 and for beam#2. With the Powershot, the images were taken in raw format and then transformed into TIFF, with a resolution equal to 2816×2112 pixels. With the EOS M3, images were captured in raw and Jpeg format and then compressed at a resolution of 50% of the original. At each load condition, a photogrammetric survey was performed, and the images were processed according to the work-flow depicted in Figure 8. The data and processing parameters of each survey are reported in Tables 9–11.

Table 9. Data and processing parameters of the CRP surveys beam#1 LC1 Powershot.

Load (kN)	No. of Images	Resolution	MB	Parameters of the Dense Point Cloud	Beam Points
0	98	2816 × 2112	2.5	Ultra-High	362,429
11	112	2816 × 2112	2.5	Ultra-High	345,251
26	114	2816 × 2112	2.5	Ultra-High	251,002
40	108	2816 × 2112	2.5	Ultra-High	316,118
54	105	2816 × 2112	2.5	Ultra-High	363,539

Table 10. Data and processing parameters of the CRP surveys beam#1 LC2 EOS M3.

Load (kN)	No. of Images	Resolution	MB	Parameters of the Dense Point Cloud	Beam Points
0	65	6000 × 4000	1	Ultra-High	1,460,945
22	55	6000 × 4000	1	Ultra-High	1,460,230
48	59	6000 × 4000	1	Ultra-High	1,459,589

Table 11. Data and processing parameters of the CRP surveys beam#2 EOS M3.

Load (kN)	No. of Images	Resolution	MB	Parameters of the Dense Point Cloud	Beam Points
0	61	6000 × 4000	1	Ultra-High	1,686,267
19	63	6000 × 4000	1	Ultra-High	1,705,513
39	53	6000 × 4000	1	Ultra-High	1,627,828
68	57	6000 × 4000	1	Ultra-High	1,733,299

The absolute orientation was established by manual collimation of the six FT# targets, thus forcing the verticality of the z axis. Tables 12–14 report the residuals of the absolute orientation on the Ground Control Points (GCPs).

Table 12. Residuals (mm) on the Ground Control Points (GCPs) beam#1 LC1 Powershot.

Load (kN)	X	Y	Z
0	1.01	1.36	0.71
11	2.62	1.34	0.69
26	0.64	0.83	0.68
40	0.70	0.60	0.33
54	3.25	5.03	2.27

Table 13. Residuals (mm) on the GCPs beam#1 LC2 condition EOS M3.

Load (kN)	X	Y	Z
0	1.44	2.87	1.07
22	0.85	1.06	0.91
48	1.30	1.18	1.11

Table 14. Residuals (mm) on the GCPs beam#2 EOS M3.

Load (kN)	X	Y	Z
0	1.61	0.97	0.64
19	1.30	1.39	0.60
39	0.83	2.01	0.55
68	1.15	1.95	1.88

The meshes were created using the Reconstructor software. The upper edges were extracted, obtaining about 1600 points for each edge, which were then used as input data for a least-squares fitting to the second-order polynomials, as was done for the TLS.

The polynomials were evaluated at the 33 sections corresponding to the target points under each load condition. Thus, the displacements were calculated by comparing the coordinates with the ones obtained at zero load.

For both calculation modes (*m2m* and *m*), the displacement values were compared with the corresponding ones obtained from the DPA and the overall RMS was assessed for each load condition.

Tables 15–17 show the RMS values for each beam and load condition and for each methodology.

Table 15. RMS (mm) in the CRP-DPA comparison beam#1 Powershot LC1.

Load (kN)	CRPCloud(<i>m2m</i>)	CRPCloud(<i>m</i>)
11	2.71	1.42
26	2.16	1.50
40	2.42	1.69
54	1.43	0.78
Global RMS	2.23	1.39

Table 16. RMS (mm) in the CRP-DPA comparison beam#1 LC2 EOS M3.

Load (kN)	CRPCloud(<i>m2m</i>)	CRPCloud(<i>m</i>)
22	1.23	0.35
48	1.08	0.89
Global RMS	1.16	0.68

Table 17. RMS (mm) in the CRP-DPA comparison beam#2 EOS M3.

Load (kN)	CRPCloud(<i>m2m</i>)	CRPCloud(<i>m</i>)
19	2.10	1.69
39	1.76	1.59
68	4.32	1.00
Global RMS	3.14	1.33

Figure 13 shows the displacements for each load and for beam#1 second load condition and for beam#2.

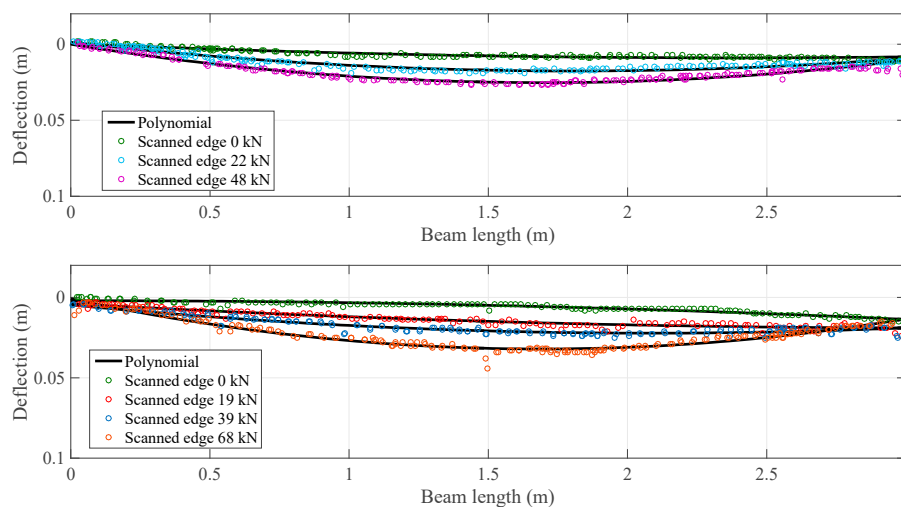


Figure 13. CRP polynomials fitted along beam span for beam#1 LC2 (top) and beam#2 (bottom). The rounded markers represent a selection of the mesh points used in the fitting process.

Figure 14 reports the comparison between the midspan displacements recorded by DPA, TLS, CRP, and DT for the three different experimental tests (beam#1 LC1, beam#1 LC2, beam#2) considering the two methodologies: $m2m$ and m .

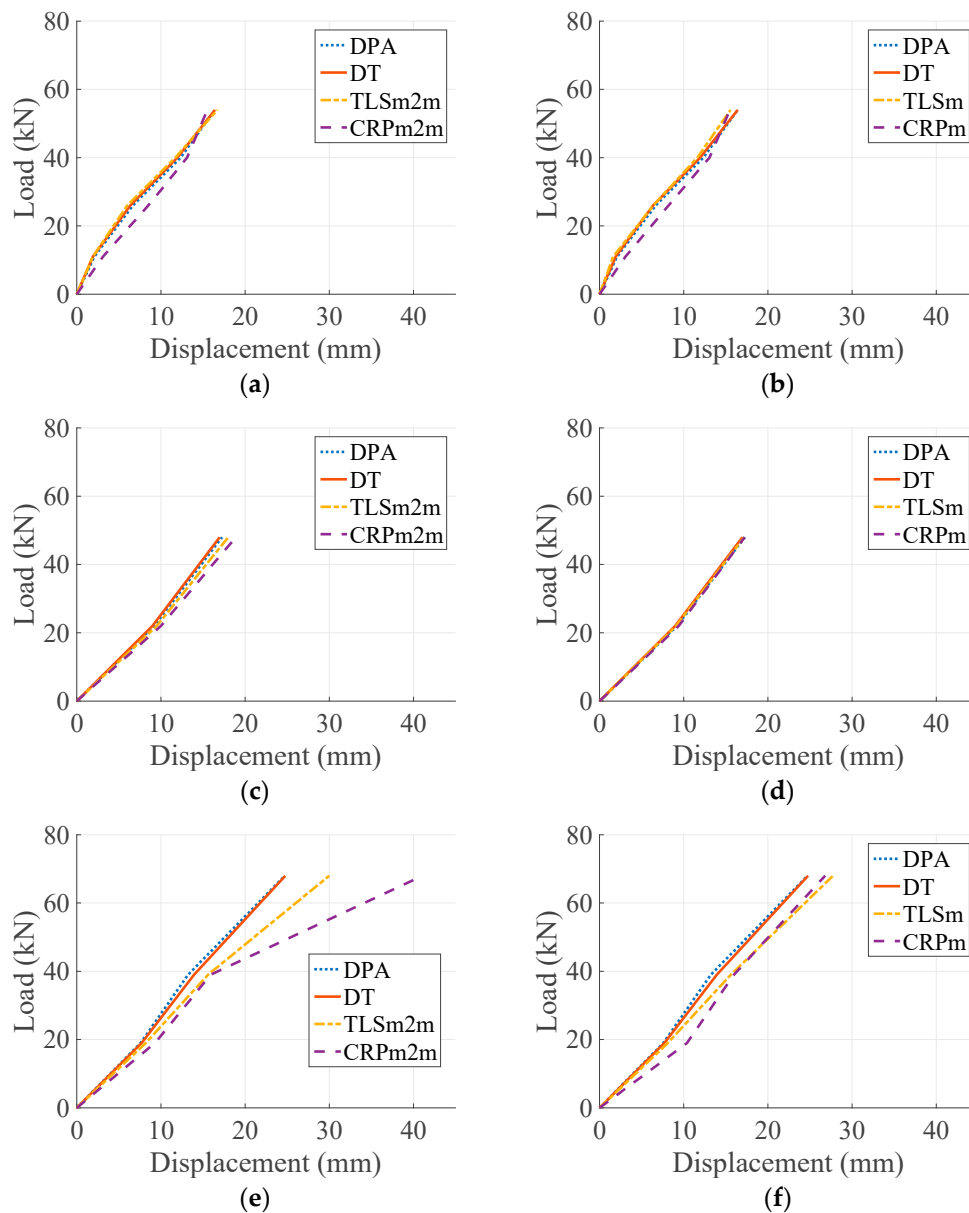


Figure 14. TLS and CRP midspan displacements comparison for beam#1 and #2. (a) beam#1 LC1 $m2m$ comparison; (b) beam#1 LC1 m comparison; (c) beam#1 LC2 $m2m$ comparison; (d) beam#1 LC2 m comparison; (e) beam#2 $m2m$ comparison; (f) beam#2 m comparison.

4. Discussion

The comparisons between the beam displacements obtained with different instruments highlighted the limitations and potential of the two adopted geomatic techniques: TLS and CRP. In particular, this paper reports on two different methodologies for extracting the metric information from the point cloud.

The results obtained with TLS using the two $m2m$ and m methodologies are similar to those obtained by Gordon [39] and Tsakiri [38] with their tests on RC and wood beams. Also, the results of the CRP are in line with some of the tests performed by Remondino [45].

In the $m2m$ case, the modeling of the point cloud is deterministic, thus the mesh is influenced by all the noise caused by the measurement and by the object's own coarseness in the measurement position, no matter what happens in the neighborhood. This behavior can explain the trend of the displacements measured by the CRP $m2m$ in Figure 14e. Indeed, looking at only this single dataset would lead to an incorrect assessment of the structural behavior of the beam.

In order to have a reliable estimation of the beam displacements, CRP data should be obtained exploiting all the available information, as happens in the polynomial modeling. Also, in order to strengthen the reliability of the calculations, groups of points whose positions are fixed and not influenced by the loads should be checked during all processes. In this study, the positions of 41 points in a stable area were monitored in each measurement series, obtaining residuals of the same order of the method accuracy.

Considering the TLS, the overall RMS obtained with the $m2m$ comparison process is 0.97 mm for the beam#1 LC1 (see Table 6), 0.96 mm for the beam#1 LC2 (see Table 7) and 0.69 mm for the beam#2 (see Table 8). Modeling the beam edge with a polynomial led to an overall RMS of 0.54 mm for the beam#1 LC1 (see Table 6), 0.92 mm for the beam#1 LC2 (see Table 7), and 0.63 mm for the beam#2 (see Table 8), with an increment of accuracy of about 20%.

Better results were obtained for the CRP: In the $m2m$ comparison, the overall RMS was 2.23 mm for the beam#1 LC1 (see Table 15), 1.16 mm for the beam#1 LC2 (see Table 16), and 3.14 for the beam#2 (see Table 17). While, if the beam edge is fitted with second-degree polynomials, the overall RMS is: 1.39 mm for the beam#1 LC1 (see Table 15), 0.68 mm for the beam#1 LC2 (see Table 16), and 1.33 mm for the beam#2 (see Table 17), with an increase in the accuracy of about 45%.

In this work, all the modeling calculations, including routines to fit portions of point clouds with respect to geometric 2D/3D shapes, were developed in the Matlab™ environment.

For the CRP test, two non-professional Canon digital cameras were used—the PowerShot S110 and the more performant EOS M3. The results obtained with the two methodologies ($m2m$ and m) were almost similar. The EOS M3 demonstrated a slightly better performance. This is definitely due to the fact that a much larger point cloud density was obtained—using a lower number of images and the same processing parameters—in the EOS M3 images compared to the PowerShot S110 images.

5. Conclusions

The goal of this research was to investigate the obtainable accuracy in the structural displacement measurements with CRP based on the Structure from Motion algorithm, and to compare this with the TLS technique. A case study on two RC beams tested under a four-points bending loading condition was presented. In order to assess the amount of displacement, point clouds at different beam loading states were acquired and compared. A complete description of the instrumentation used and the experimental environment, along with a comprehensive report on the calculations and results obtained was reported. Two kinds of point clouds comparison were investigated: Mesh to mesh ($m2m$) and modeling (m), with simple geometric primitives as second-order polynomials.

The comparison between the $m2m$ and the m approaches showed that the latter leads to significantly better results for both TLS and CRP.

The results obtained with the TLS for both the $m2m$ and m methodologies present RMS below 1 mm; while for CRP, the RMS is around a few millimeters for $m2m$ and around 1 mm for m .

The CRP results were highly accurate for two main reasons: The distance between the instruments and the beam was quite short (3–4 m, see Figure 6) with a very small GSD; the dimensional scale of the photogrammetric images was obtained through laser tracker measurements. This last approach is not typical when working in the field, but the problem can be overcome by introducing two or more calibrated scale bars.

The obtained results allow for consideration of these two techniques, which are suitable to evaluate the deformation of structures. Both tested techniques can be considered fast and effective, but the difference in cost should be highlighted. On the one hand, the TLS cost is quite high, both in terms of

instrumentation and data processing software; while on the other hand, the CRP can be developed with non-professional digital cameras at an affordable cost and low-cost commercial or open-source software can be used for the image processing and point clouds management.

Further developments are expected considering both new analyses of the already obtained experimental data and new field tests considering larger structures and longer distances between instruments and measured objects. Indeed, the techniques adopted in this paper to reduce the uncertainty of the coordinates of the photogrammetric point clouds can be used when it is necessary to accurately know the dimensions of structures such as steel pylons. In addition, the image processing techniques with subpixel capabilities, see [61–64], seem very promising for structural health monitoring.

Author Contributions: F.S. and F.M. developed the structural part while G.S. and G.V. performed the geomatic survey. The geomatic and metrological analysis were developed by G.S. and G.V. All the authors wrote the paper.

Funding: This study was supported by the research grant for the project “Healthy Cities and Smart Territories” (2016/17) funded by Fondazione di Sardegna and the Autonomous Region of Sardinia. Flavio Stochino acknowledges the financial support of the Autonomous Region of Sardinia under grant P.O.R. SARDEGNA 2014–2020, CCI: 2014- IT05SFOP021, Project: Retrofitting, rehabilitation and requalification of the historical cultural architectural 506 heritage (R3-PAS).

Conflicts of Interest: The authors declare no conflict of interest.

References

1. Mechelke, K.; Sternberg, H.; Keller, F. A monitoring system with TLS sensor. In Proceedings of the Joint International Symposium on Deformation Monitoring, Nottingham, UK, 9–10 September 2013.
2. Meloni, P.; Mistretta, F.; Stochino, F.; Carcangiu, G. Thermal Path Reconstruction for Reinforced Concrete Under Fire. *Fire Technol.* **2019**, in press. [[CrossRef](#)]
3. Stochino, F.; Mistretta, F.; Meloni, P.; Carcangiu, G. Integrated Approach for Post-fire Reinforced Concrete Structures Assessment. *Period. Polytech. Civ. Eng.* **2017**, *61*, 677–699. [[CrossRef](#)]
4. Vacca, G.; Mistretta, F.; Stochino, F.; Dessi, A. Terrestrial Laser Scanner for monitoring the deformations and the damages of buildings. *Int. Arch. Photogramm. Remote Sens. Spatial Inf. Sci.* **2016**, *XLI-B5*, 453–460. [[CrossRef](#)]
5. Giresini, L.; Sassu, M. Tests Results and Simple Structural Analysis of the Main Lighthouse in the Harbor of Livorno (Italy). *Adv. Mater. Res.* **2014**, *834*, 1299–1303. [[CrossRef](#)]
6. Stochino, F.; Fadda, M.L.; Mistretta, F. Assessment of RC bridges integrity by means of low-cost investigations. *Frat. Ed Integrita Strutt. (Fract. Struct. Integr.)* **2018**, *12*, 216–225. [[CrossRef](#)]
7. Pucci, A.; Puppio, M.L.; Giresini, L.; Sousa, H.; Matos, J.; Sassu, M. Method for sustainable large-scale bridges survey. In *Towards a Resilient Built Environment Risk and Asset Management*; International Association for Bridge and Structural Engineering: Guimarães, Portugal, 2019; pp. 1034–1041.
8. Han, J.; Guo, J.; Jiang, Y. Monitoring tunnel profile by means of multi-epoch dispersed 3-D LIDAR point clouds. *Tunn. Undergr. Space Technol.* **2013**, *33*, 186–192. [[CrossRef](#)]
9. Deidda, M.; Sanna, G. Integration of Geomatics Techniques for the Urban Cavity Survey. *ISPRS Ann. Photogramm. Remote Sens. Spatial Inf. Sci.* **2013**, *II-5/W1*, 91–96. [[CrossRef](#)]
10. Kasperski, J.; Delacourt, C.; Allemand, P.; Potherat, P.; Jaud, M.; Varrel, E. Application of a terrestrial laser scanner (TLS) to the study of the Séchilienne Landslide (Isère, France). *Remote Sens.* **2010**, *2*, 2785–2802. [[CrossRef](#)]
11. Xu, Z.; Wu, L.; Shen, Y.; Li, F.; Wang, Q.; Wang, R. Tridimensional reconstruction applied to cultural heritage with the use of camera-equipped UAV and terrestrial laser scanner. *Remote Sens.* **2014**, *6*, 10413–10434. [[CrossRef](#)]
12. Giresini, L.; Gioeli, A.; Sassu, M. Seismic Reinforcement of a RC Building with External Steel Frameworks: The Case of the Primary School XXV April of Arcola (Italy). *Adv. Mater. Res.* **2014**, *834*, 697–700.
13. Sassu, M.; Andreini, M.; De Falco, A.; Giresini, L.; Puppio, M.L. Structural protection after landslide phenomena: A case study in Northern Italy. In *Civil Engineering and Urban Planning IV, Proceedings of the 4th International Conference on Civil Engineering and Urban Planning, Beijing, China, 25–27 July 2015*; Liu, Y.M., Fu, D., Tong, Z.X., Bao, Z.Q., Tang, B., Eds.; CRC Press: Boca Raton, FL, USA, 2016; pp. 241–246.

14. Giannattasio, C.; Grillo, S.M.; Vacca, G. Interdisciplinary study for knowledge and dating of the San Francesco convent in Stampace, Cagliari—Italy (XIII–XXI century). *ISPRS Ann. Photogramm. Remote Sens. Spatial Inf. Sci.* **2013**, *II-5/W1*, 139–144. [[CrossRef](#)]
15. Stochino, F.; Fadda, M.L.; Mistretta, F. Low cost condition assessment method for existing RC bridges. *Eng. Fail. Anal.* **2018**, *86*, 56–71. [[CrossRef](#)]
16. Lindenbergh, R.; Pietrzyk, P. Change detection and deformation analysis using static and mobile laser scanning. *Appl. Geomat.* **2017**, *7*, 65–74. [[CrossRef](#)]
17. Mukupa, W.; Roberts, G.W.; Hancock, C.M.; Al-Manasir, K. A review of the use of terrestrial laser scanning application for change detection and deformation monitoring of structures. *Surv. Rev.* **2017**, *49*, 99–116. [[CrossRef](#)]
18. Vosselman, G.; Maas, H.G. *Airborne and Terrestrial Laser Scanning*; Whittles Publishing: Dunbeath, UK, 2010.
19. Lague, D.; Brodu, N.; Leroux, J. Accurate 3D comparison of complex topography with terrestrial laser scanner: Application to the Rangitikei canyon (N-Z). *ISPRS J. Photogramm. Remote Sens.* **2013**, *82*, 10–16. [[CrossRef](#)]
20. Rutzinger, M.; RUF, B.; Höfle, B.; Vetter, M. Change detection of building footprints from airborne laser scanning acquired in short time intervals. *Int. Arch. Photogramm. Remote Sens. Spat. Inf. Sci.* **2010**, *38*, 475–480.
21. Xu, S.; Vosselman, G.; Oude Elberink, S. Detection and classification of changes in buildings from airborne laser scanning data. *ISPRS Ann. Photogramm. Remote Sens. Spat. Inf. Sci.* **2013**, *II-5/W2*, 343–348. [[CrossRef](#)]
22. Pesci, A.; Teza, G.; Bonali, E.; Casula, G.; Boschi, E. A laser-scanning based method for fast estimation of seismic-induced building deformations. *ISPRS J. Photogramm. Remote Sens.* **2013**, *79*, 185–198. [[CrossRef](#)]
23. Wang, T.; Jaw, J.; Chang, Y.; Jeng, F. Application and validation of profile-image method for measuring deformation of tunnel wall. *Tunn. Undergr. Space Technol.* **2009**, *24*, 136–147. [[CrossRef](#)]
24. Wujanz, D.; Neitzel, F.; Hebel, H.P.; Linke, J.; Busch, W. Terrestrial radar and laser scanning for deformation monitoring: First steps towards assisted radar scanning. *ISPRS Ann. Photogramm. Remote Sens. Spat. Inf. Sci.* **2013**, *II(5/W2)*, 325–330. [[CrossRef](#)]
25. Hanssen, R.F. *Radar Interferometry*; Kluwer Academic Publishers: Dordrecht, The Netherlands, 2001.
26. Bremer, M.; Sass, O. Combining airborne and terrestrial laser scanning for quantifying erosion and deposition by a debris flow event. *Geomorphology* **2012**, *138*, 49–60. [[CrossRef](#)]
27. Young, A.P.; Olsen, M.J.; Driscoll, N.; Flick, R.; Gutierrez, R.; Guza, R.; Johnstone, E.; Kuester, F. Comparison of airborne and terrestrial lidar estimates of seacliff erosion in southern california. *Photogramm. Eng. Remote Sens.* **2010**, *76*, 421–427. [[CrossRef](#)]
28. Olsen, M.; Kuester, F.; Chang, B.; Hutchinson, T. Terrestrial laser-scanning-based structural damage assessment. *J. Comput. Civ. Eng.* **2010**, *24*, 264–272. [[CrossRef](#)]
29. Pesci, A.; Casula, G.; Boschi, E. Laser scanning the Garisenda and Asinelli towers in Bologna (Italy): Detailed deformation patterns of two ancient leaning buildings. *J. Cult. Herit.* **2011**, *12*, 117–127. [[CrossRef](#)]
30. Riveiro, B.; Arias, P.; Armesto, J.; Rial, F.; Solla, M. Multidisciplinary approach to historical arch bridges documentation. *Int. Arch. Photogramm. Remote Sens. Spat. Inf. Sci.* **2008**, *XXXVII(B5)*, 247–252.
31. Grosse-Schwiep, M.; Piechel, J.; Luhmann, T. Measurement of rotor blade deformations of wind energy converters with laser scanners. *ISPRS Ann. Photogramm. Remote Sens. Spat. Inf. Sci.* **2013**, *II(5/W2)*, 97–102. [[CrossRef](#)]
32. Scaioni, M.; Marsella, M.; Crosetto, M.; Tornatore, V.; Wang, J. Geodetic and Remote-Sensing Sensors for Dam Deformation Monitoring. *Sensors* **2018**, *18*, 3682. [[CrossRef](#)] [[PubMed](#)]
33. Jaafar, H.A.; Meng, X.; Sowter, A. Terrestrial laser scanner error quantification for the purpose of monitoring. *Surv. Rev.* **2017**. [[CrossRef](#)]
34. Zhao, P.; Hu, Q.; Wang, S.; Ai, M.; Mao, Q. Panoramic Image and Three-Axis Laser Scanner Integrated Approach for Indoor 3D Mapping. *Remote Sens.* **2018**, *10*, 1269. [[CrossRef](#)]
35. Park, H.S.; Lee, H.M.; Adeli, H.; Lee, I. A new approach for health monitoring of structures: Terrestrial laser scanning. *Comput. Aided Civ. Infrastruct. Eng.* **2007**, *22*, 119–130. [[CrossRef](#)]
36. Girardeau-Montaut, D.; Roux, M.; Marc, R.; Thibault, G. Change detection on points cloud data acquired with a ground laser scanner. *Int. Arch. Photogramm. Remote Sens. Spat. Inf. Sci.* **2005**, *36*, 30–35.
37. Xu, X.; Bureick, J.; Yang, H.; Neumann, I. TLS-based composite structure deformation analysis validated with laser tracker. *Compos. Struct.* **2018**, *202*, 60–65. [[CrossRef](#)]

38. Tsakiri, M.; Lichti, D.; Pfeifer, N. Terrestrial laser scanning for deformation monitoring. In Proceedings of the 3rd IAG/12th FIG Symposium, Baden, Germany, 22–24 May 2006.
39. Gordon, G.; Lichti, D.D.; Franke, J.; Stewart, M.P. Measurement of structural deformation using terrestrial laser scanners. In Proceedings of the 1st FIG International Symposium on Engineering Surveys for Construction Works and Structural Engineering, Nottingham, UK, 28 June–1 July 2004.
40. Luhmann, T.; Robson, S.; Kyle, S.; Boehm, J. *Close Range Photogrammetry: 3D Imaging Techniques*; Walter De Gruyter Inc.: Berlin, Germany, 2014.
41. Szeliski, R. *Computer Vision: Algorithms and Applications*; Springer: Berlin, Germany, 2010.
42. Mancini, F.; Dubbini, M.; Gattelli, M.; Stecchi, F.; Fabbri, S.; Gabbianelli, G. Using Unmanned Aerial Vehicles (UAV) for High-Resolution Reconstruction of Topography: The Structure from Motion Approach on Coastal Environments. *Remote Sens.* **2013**, *5*, 6880–6898. [[CrossRef](#)]
43. Mathews, A.; Jensen, J. Visualizing and quantifying vineyard canopy LAI using an unmanned aerial vehicle (UAV) collected high density structure from motion point cloud. *Remote Sens.* **2013**, *5*, 2164–2183. [[CrossRef](#)]
44. Turner, D.; Lucieer, A.; Watson, C. An automated technique for generating georectified mosaics from ultra-high resolution unmanned aerial vehicle (UAV) imagery, based on structure from motion (SfM) point clouds. *Remote Sens.* **2012**, *4*, 1392–1410. [[CrossRef](#)]
45. Remondino, F.; Spera, M.G.; Nocerino, E.; Menna, F.; Nex, F. State of the art in high density image matching. *Photogramm. Rec.* **2014**, *29*, 144–166. [[CrossRef](#)]
46. Swinfield, T.; Lindsell, J.A.; Williams, J.V.; Harrison, R.D.; Habibi, A.; Gemita, E.; Schönlieb, C.B.; Coomes, D.A. Accurate Measurement of Tropical Forest Canopy Heights and Aboveground Carbon Using Structure from Motion. *Remote Sens.* **2019**, *11*, 928. [[CrossRef](#)]
47. Jiang, Q.; Fang, S.; Peng, Y.; Gong, Y.; Zhu, R.; Wu, X.; Ma, Y.; Duan, B.; Liu, J. UAV-Based Biomass Estimation for Rice-Combining Spectral, TIN-Based Structural and Meteorological Features. *Remote Sens.* **2019**, *11*, 890. [[CrossRef](#)]
48. Ni, W.; Dong, J.; Sun, G.; Zhang, Z.; Pang, Y.; Tian, X.; Li, Z.; Chen, E. Synthesis of Leaf-on and Leaf-off Unmanned Aerial Vehicle (UAV) Stereo Imagery for the Inventory of Aboveground Biomass of Deciduous Forests. *Remote Sens.* **2019**, *11*, 889. [[CrossRef](#)]
49. Morgan, J.A.; Brogan, D.J.; Nelson, P.A. Application of Structure-from-Motion photogrammetry in laboratory flumes. *Geomorphology* **2017**, *276*, 125–143. [[CrossRef](#)]
50. Grillo, S.M.; Pilia, E.; Vacca, G. Integrated study of the Beata Vergine Assunta dome with structure from motion and diagnostic approaches. *Int. Arch. Photogramm. Remote Sens. Spat. Inf. Sci.* **2019**, *XLII-2/W11*, 579–585. [[CrossRef](#)]
51. Kersten, T.P.; Lindstaedt, M. Automatic 3D object reconstruction from multiple images for architectural, cultural heritage and archaeological applications using open-source software and web services. *Photogramm. Fernerkund. Geoinf. (PFG)* **2012**, *6*, 727–740. [[CrossRef](#)]
52. Remondino, F.; Del Pizzo, S.; Kersten, T.P.; Troisi, S. Low-cost and open-source solutions for automated image orientation a critical overview. In *Progress in Cultural Heritage Preservation*; Springer: Berlin/Heidelberg, Germany, 2012; pp. 40–54.
53. Barazzetti, L.; Scaioni, M. Development and implementation of image-based algorithms for measurement of deformations in material testing. *Sensors* **2010**, *10*, 7469–7495. [[CrossRef](#)] [[PubMed](#)]
54. Barazzetti, L.; Scaioni, M. Crack measurement: Development, testing and applications of an automatic image-based algorithm. *ISPRS J. Photogramm. Remote Sens.* **2009**, *64*, 285–296. [[CrossRef](#)]
55. Deiana, G.L.; Dessi, A.; Mistretta, F.; Sanna, G.; Stochino, F.; Urru, E.; Vacca, G.; Valdes, M. Terrestrial Laser Scanner and Close Range Photogrammetry point clouds accuracy assessment for the structure deformations monitoring. In *Geospatial Information for a Smarter Life and Environmental Resilience, Proceedings of the FIG Working Week*; Fédération Internationale des Géomètres (FIG): Hanoi, Vietnam, 2019.
56. Agisoft Software. Available online: <http://www.agisoft.com/> (accessed on 10 January 2019).
57. Photoscan Manual. Available online: http://www.agisoft.com/pdf/photoscan-pro_1_3_en.pdf (accessed on 10 January 2019).
58. Westoby, M.; Brasington, J.; Glasser, N.F.; Hambrey, M.J.; Reynolds, J.M. ‘Structure from-motion’ photogrammetry: A low-cost, effective tool for geoscience applications. *Geomorphology* **2012**, *179*, 300–314. [[CrossRef](#)]

59. Fonstad, M.A.; Dietrich, J.T.; Courville, B.C.; Jensen, J.L.; Carbonneau, P.E. Topographic structure from motion: A new development in photogrammetric measurement. *Earth Surf. Process. Landf.* **2013**, *38*, 421–430. [[CrossRef](#)]
60. Fathi, H.; Dai, F.; Lourakis, M. Automated as-built 3D reconstruction of civil infrastructure using computer vision: Achievements, opportunities, and challenges. *Adv. Eng. Inform.* **2015**, *29*, 149–161. [[CrossRef](#)]
61. Chen, J.G.; Wadhwa, N.; Cha, Y.J.; Durand, F.; Freeman, W.T.; Buyukozturk, O. Modal identification of simple structures with high-speed video using motion magnification. *J. Sound Vib.* **2015**, *345*, 58–71. [[CrossRef](#)]
62. Mas, D.; Espinosa, J.; Roig, A.B.; Ferrer, B.; Perez, J. Image based subpixel techniques for movement and vibration tracking. In Proceedings of the 11th European conference on non-destructive testing (ECNDT 2014), Prague, Czech Republic, 6 October 2014.
63. Zhang, D.; Guo, J.; Lei, X.; Zhu, C. A high-speed vision-based sensor for dynamic vibration analysis using fast motion extraction algorithms. *Sensors* **2016**, *16*, 572. [[CrossRef](#)]
64. Javh, J.; Slavič, J.; Boltežar, M. The subpixel resolution of optical-flow-based modal analysis. *Mech. Syst. Signal Process.* **2017**, *88*, 89–99. [[CrossRef](#)]



© 2019 by the authors. Licensee MDPI, Basel, Switzerland. This article is an open access article distributed under the terms and conditions of the Creative Commons Attribution (CC BY) license (<http://creativecommons.org/licenses/by/4.0/>).